

# The milliDelta: A High-Bandwidth, High-Precision, Millimeter-Scale Delta Robot

Hayley McClintock<sup>1\*</sup>, F. Zeynep Temel<sup>1\*</sup>, Neel Doshi<sup>1</sup>,  
Je-sung Koh<sup>1,2</sup>, Robert J. Wood<sup>1</sup>

\*Both authors contributed equally

<sup>1</sup>John A. Paulson School of Engineering and Applied Sciences and  
Wyss Institute for Biologically Inspired Engineering,  
Harvard University, Cambridge, MA 02138, USA

<sup>2</sup>Department of Mechanical Engineering, Ajou University, South Korea

\*To whom correspondence should be addressed; E-mail: [hayley.mcclintock@wyss.harvard.edu](mailto:hayley.mcclintock@wyss.harvard.edu),  
[fztemel@seas.harvard.edu](mailto:fztemel@seas.harvard.edu), [ndoshi@seas.harvard.edu](mailto:ndoshi@seas.harvard.edu),  
[jskoh@ajou.ac.kr](mailto:jskoh@ajou.ac.kr), [rjwood@seas.harvard.edu](mailto:rjwood@seas.harvard.edu)

**Delta robots have been widely used in industrial contexts for pick-and-place applications due to their high precision and speed. These qualities are also desirable at the millimeter scale for applications such as vibration cancellation in microsurgery and microassembly, or micromanipulation. Developing a millimeter-scale Delta robot that maintains the characteristic input-output behavior and operates with high speed and precision requires overcoming manufacturing and actuation challenges. Here, we present the design, fabrication, and characterization of an adapted Delta robot at the millimeter scale (the “milliDelta”) that leverages PC-MEMS manufacturing techniques and is driven by three independently controlled piezoelectric bending actuators. We**

**validate the design of the milliDelta, where two non-intersecting perpendicular revolute joints are used to replace an ideal universal joint. In addition, a transmission linkage system for actuation is introduced to the laminate structure of the milliDelta. This  $15\text{ mm} \times 15\text{ mm} \times 20\text{ mm}$  robot has a total mass of 430 mg, a payload capacity of 1.31 g, and operates with precision down to  $\sim 5\text{ }\mu\text{m}$  in a  $7.01\text{ mm}^3$  workspace. Additionally, the milliDelta can follow periodic trajectories at frequencies up to 75 Hz, experiencing velocities of  $\sim 0.45\text{ m/s}$  and accelerations of  $\sim 22g$ . These characteristics make it the smallest and highest frequency Delta robot to date, and we demonstrate its potential utility for high bandwidth, high precision applications that require a compact design.**

## Introduction

Parallel manipulators exhibit many favorable characteristics, including high speeds and accelerations, low inertias, high stiffnesses, and superior precision relative to serial manipulators (1–3). In 1990, Clavel introduced the Delta robot (4–6), a 3 degree-of-freedom (DOF) parallel mechanism motivated by the need for a pick-and-place tool in a chocolate factory (7). In addition to the traditional advantages of parallel manipulators, the Delta robot provides decoupling between the orientation and translation of the end effector (3–6) and has simple closed-form kinematic solutions (1, 6, 8, 9). This is a marked improvement over earlier parallel mechanism designs which suffered from limited workspaces, complicated mechanical design, and complex kinematics (3, 6, 10, 11). For these reasons, Delta robots are widely used in industrial applications such as food packaging, machining, welding, and pick-and-place assembly (2, 3, 6, 12). The advantages of the Delta robot design, including a low inertia that allows for high speed and acceleration, improve as size decreases, making it a desirable design for small scale applications such as microassembly, micromanipulation, and medical robotics (13–16). For these applica-

**Table 1:** Relevant parameters for a selection of currently available Delta robots.

| Device                     | Size (mm)                 | Weight (g) | Workspace (mm <sup>3</sup> ) | Frequency (Hz) | Payload (N) | Accuracy (μm) |
|----------------------------|---------------------------|------------|------------------------------|----------------|-------------|---------------|
| IRB 360 FlexPicker (20)    | 565 radius<br>1000 height | 120000     | 395500                       | ~3             | ~78         | 100           |
| Adept Quattro s650HS (20)  | 650 radius<br>1150 height | 117000     | 650000                       | 5              | ~59         | 100           |
| Pocket Delta (20)          | 171×171 ×270              | 5.6        | 4050                         | 2              | 0.2         | 3             |
| Laminated Delta Robot (18) | ~100×100 ×100             | –          | ~700                         | –              | 1           | 100           |
| milliDelta                 | 15×15×20                  | 0.430      | 7.01                         | 75             | .0131       | 5             |

tions, there has been development in the design and fabrication of Delta robots with workspaces tailored to this scale (13–18). These robots demonstrate the scalability of the Delta robot design, but are still at the meso-scale (~10 cm). While these designs often couple traditional manufacturing techniques (13, 15, 19) with novel flexure design (15, 17, 18), an integrated approach to design and fabrication must be used in order to achieve a millimeter-scale Delta robot for better incorporation into devices, such as surgical tools, as an end effector.

For developing robots at the millimeter scale, Smart Composite Micro-structures (SCM) and Printed-Circuit MEMS (PC-MEMS) enable the fabrication of highly articulated 3D structures (21–24). Leveraging these design and fabrication techniques, high performance composite materials, and zero-backlash flexural joints, complex mechanisms, such as those found in parallel manipulators, can be realized at the millimeter scale. Using a laminate structure also yields advantages such as scalability, reduced cost, and improved performance (25). For example, dimensional parameters can easily be adjusted for meso- to micro-scale applications. Finally, millimeter-scale laminate structures require less maintenance than traditionally manufactured devices as a result of fewer moving parts (25).

Various actuators exist at the millimeter scale, including rotary motors (26), soft micro-

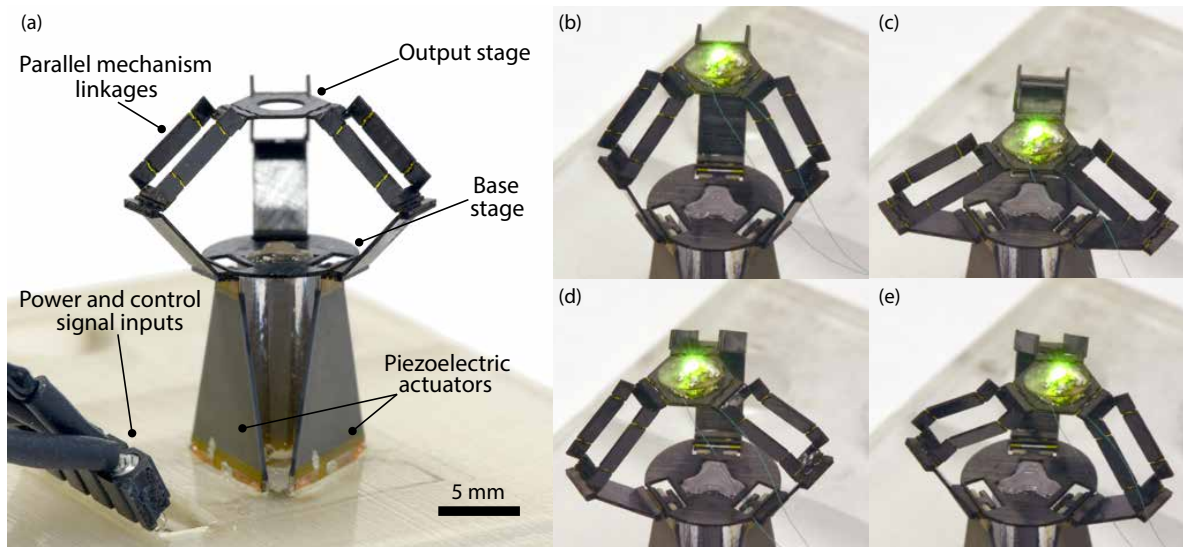


**Figure 1:** (A) The milliDelta with components labeled. Design of the milliDelta is based on origami-inspired engineering and made using PC-MEMS manufacturing techniques. The robot is driven by three piezoelectric bending actuators. Power and control signals are delivered via a five wire tether. Perspective views of the milliDelta moving through its workspace near the top (B), bottom (C), left (D), and right (E) with externally powered LED for visualization.

actuators (27, 28), voice coil actuators (17, 26), and piezoelectric actuators (26, 29–31). However, rotary motors function poorly due to surface effects (18, 26, 32), microfluidic actuators are limited in their maximum operational frequency (27), and voice coil actuators require suspension (17, 26). Due to their high (kilohertz) bandwidth, high power density, and low profile, piezoelectric bending actuators are well suited to power motion in millimeter-scale devices (29–31, 33–35). Using piezoelectric actuators enables devices to be scaled down significantly and increases their maximum operational frequency.

In this paper we present the milliDelta, a 15 mm×15 mm×20 mm Delta robot (Fig. 1) based on the PC-MEMS manufacturing technique and driven by piezoelectric bending actuators. We modify the design of the conventional Delta robot for monolithic fabrication and develop custom fixtures for improved assembly and actuator integration. These modifications are validated and the characterization of the milliDelta’s workspace, payload capacity, bandwidth, precision, and accuracy are described in the Results section. The milliDelta has a mass of 430 mg (60 mg linkage mass and 370 mg actuator mass) and achieves a maximum workspace of 7.01 mm<sup>3</sup> with a payload capacity of 1.31 g ( $\sim 3 \times$  its mass). Additionally, piezoelectric bending actuators enable operation at frequencies up to 75 Hz, which to the best of the authors’ knowledge, is 15–25× higher bandwidth than any Delta robot currently available (20).

The scalability and small size of the milliDelta make it a good candidate to replace bulky mechanical structures in millimeter-scale robotic applications that require high precision and accuracy, including micropositioning stages, novel wrist mechanisms for robotic arms, and micromanipulation and micro-scale pick-and-place applications. We demonstrate the robot’s precision ( $\sim 5 \mu\text{m}$  RMS) when tracking complex trajectories and performing high speed motions. Though other micro-manipulators developed at this scale are precise down to 0.1  $\mu\text{m}$ , no other designs are able to reach frequencies as high as the milliDelta (15, 16, 36), which enables rapid automation in micro assembly tasks and microfabrication systems. Additionally, due to reduced

cost from miniaturization, the milliDelta can be used as a (potentially disposable) end effector in medical devices. For example, the milliDelta can be used for tremor compensation, and we show its ability to reduce hand tremors by 81% using open loop compensation. This reduction is comparable to that of similar, fully integrated vibration cancellation devices (also between 80-90% (37)), table-top surgical systems (38), and close to that of surgical robots teleoperated by surgeons (39).

## Results

### Design

Conventional Delta robots consist of two parallel plates; the fixed base and the moving output stage, connected by three kinematic chains (2, 7, 40). Each chain is driven by a single DOF actuator connected to the fixed base. The base arm linkage transmits the motion to two parallel bars that are connected to the output stage (7). These parallel bars form a parallelogram structure that is key for the functionality of the Delta robot (7). The joints between the base arm linkage, parallelogram, and the output stage are universal joints.

The milliDelta (Fig. 2) is designed using 3D CAD software (SolidWorks) and custom laminate design software “popupCAD” (42). The rotational joints at the fixed base of the Delta robot are replaced with revolute flexural joints, with an inherent stiffness and damping (43). Each of the six universal joints is separated into two perpendicular revolute flexural joints as shown in Fig. 2D. The perpendicular revolute joints provide 2-DOF rotation about two perpendicular axes, approximating a universal joint as discussed in Design Verification. Furthermore, assembly flexural joints fixed at an angle of 45° are introduced to keep the moving flexural joints unloaded at the center of the milliDelta’s workspace (Fig. S2C).

Three additional input linkages, crank-sliders in series with a linearizing revolute flexural

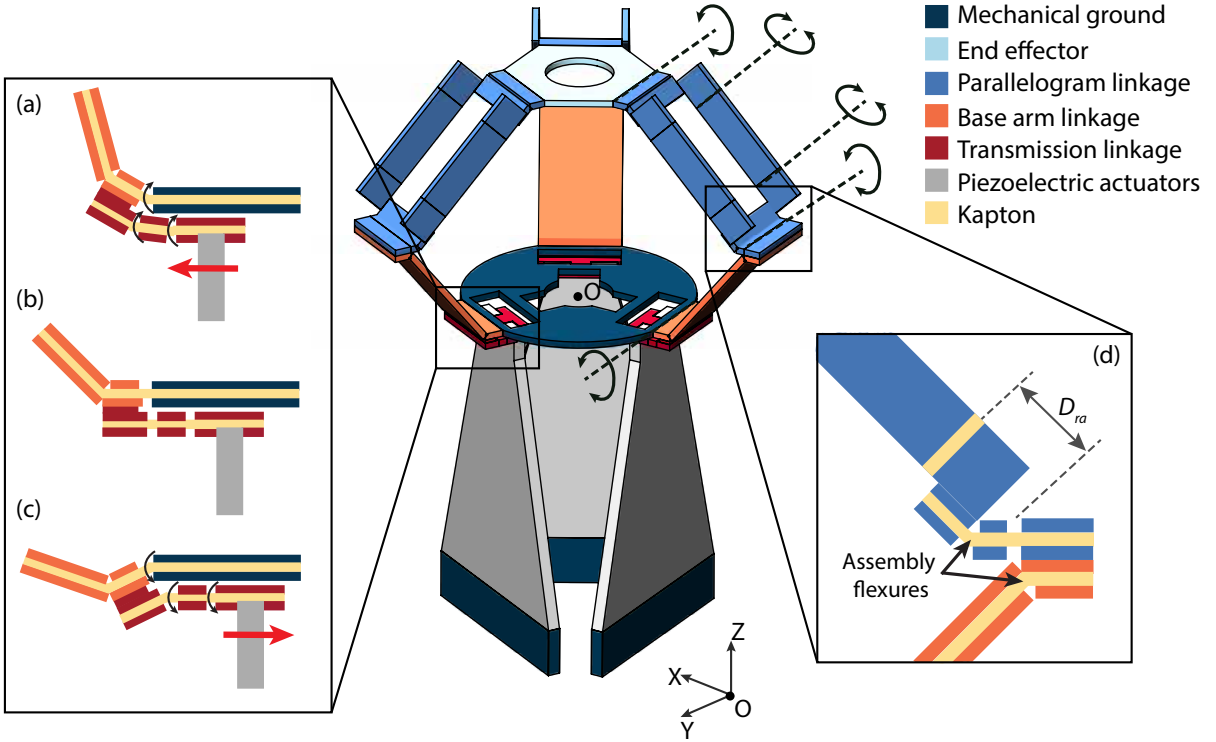


**Figure 2:** Schematic representation of the milliDelta. Revolute joint axes are labeled with dashed black lines, and the composite laminate structure is shown with the flexible polyimide and rigid layers as described in the legend. The milliDelta has two parallel plates (the fixed base and the output stage) that are connected by three kinematic chains driven by piezoelectric bending actuators. Three additional input transmission linkages are added to convert and amplify (by  $1/L_3$ ) the bending motion (red arrow) of the actuators to rotary motion at the fixed base (black arrow). Input transmission linkages are shown in upper (A), neutral (B), and lower (C) configurations as in (41). (D) Universal joints conventionally present at the fixed base and at the output stage are approximated with two perpendicular revolute joints separated by distance  $D_{ra}$ . Assembly flexural joints fixed at an angle of  $45^\circ$  are introduced to keep the moving flexural joints unloaded at the center of the milliDelta's workspace.

joint, as described in (41), are added to the milliDelta (Fig. 2A-C). These transmissions convert and amplify the bending input motion of the piezoelectric actuators to a rotary motion of the revolute flexural joints at the fixed base. The amplification (transmission ratio) is determined by  $1/L_3$  (labeled in Fig. 2B and Fig. S1). Piezoelectric bending actuators can be modeled as a force source proportional to the magnitude of the input voltage in parallel with a nonlinear spring (29). The peak-to-peak input voltage and the actuator tip deflection are limited to  $\sim 225$  V ( $1.7 \mu\text{m}/\text{V}$  field) and  $\sim 600 \mu\text{m}$ , respectively, to increase lifetime (29). Given these considerations, the models presented in (29) and (41) are used in an iterative experimental procedure to determine input linkage lengths, actuator dimensions, and flexural stiffnesses to achieve approximately  $\pm 45^\circ$  of rotation (see Table S1 and Fig. S1).

### Design Verification

Ideal universal joints, as found in conventional Delta robots, can be realized for laminate manufacturing using a spherical-five-bar linkage system with two coincident rotational axes (44). However, the complexity of this linkage system can introduce manufacturing errors in small scale devices, specifically when manual assembly is required. To reduce this error in the design of the milliDelta, two perpendicular revolute joints with offset axes of rotation are used to approximate ideal universal joints (Fig. 2D).

To understand the effect of this axis bias on the motion of the milliDelta's output stage, a simulation study is performed using the kinematic model described in Material and Methods. For this study, three workspaces are calculated using different bias distances between the rotational axes of the approximated universal joints,  $D_{ra}$  (Fig. 2D). The milliDelta has a  $D_{ra}$  of 0.8 mm. Its workspace is compared to that of a conventional Delta robot ( $D_{ra} = 0$  mm) and a  $2\times$  bias case ( $D_{ra} = 1.6$  mm), with all other dimensional parameters and inputs kept constant (Fig. 3). As  $D_{ra}$  increases, an anisotropic change occurs in the workspace; the coverage de-

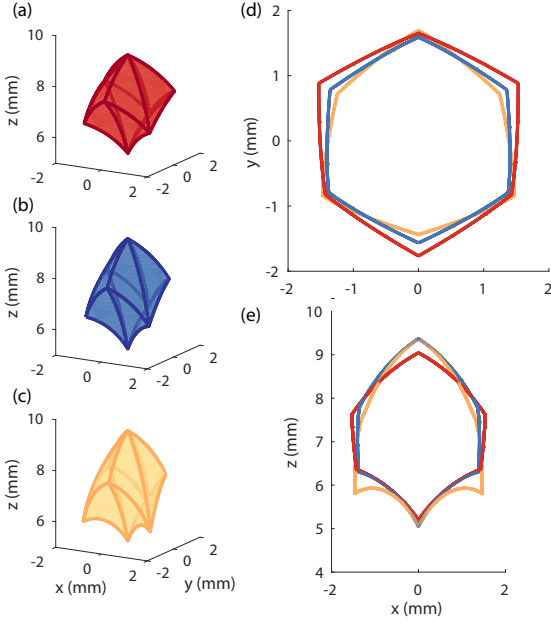


**Figure 3:** Workspace comparison of (A) a conventional Delta robot design ( $D_{ra} = 0$  mm), (B) the milliDelta ( $D_{ra} = 0.8$  mm), and (C) a Delta robot with 2x axis bias ( $D_{ra} = 1.6$  mm). The xy projection of the workspaces is shown in (D) and the xz projection is shown in (E).

creases in the xy-plane and increases in the xz-plane. Using actuator input deflections of  $\pm 70 \mu\text{m}$ , the workspace volumes of the conventional design, the milliDelta, and the  $2\times$  bias case are calculated as  $7.30 \text{ mm}^3$ ,  $7.17 \text{ mm}^3$ , and  $7.86 \text{ mm}^3$ , respectively. These deviations are relatively minor (7.5%), demonstrating that two non-intersecting perpendicular revolute joints can be used to replace an ideal universal joint in manufacturing microrobots with PC-MEMS techniques.

## Quasi-static Characterization

### Workspace Measurements

The experimental workspace characterization is performed using the experimental setup in Fig. 8 to record the position of the output stage of the milliDelta. Eighteen actuation schemes are tested to determine the extent of the milliDelta's workspace (Fig. 4). While performing these workspace motions, the milliDelta exhibits an average RMS deviation from the mean trajectory

of  $4.6 \pm 0.9 \mu\text{m}$  ( $n=18$  trials). These trajectories are displayed in Fig. 4 alongside the kinematic model's predictions based on the average observed actuator deflection ( $\sim \pm 70 \mu\text{m}$ ). In order to calculate the total workspace of the milliDelta, a polynomial fit is used to create a 3D volume ( $7.01 \text{ mm}^3$ ). The experimental workspace closely matches the predicted workspace both in shape and volume. The difference between the kinematic and experimental workspaces is calculated as  $0.16 \text{ mm}^3$  ( $\sim 1\%$ ), and is likely due to fabrication errors and material imperfections that cause asymmetries between arms. These discrepancies can be reduced using pop-up fabrication to eliminate manual assembly (see Materials and Methods), and more sophisticated system identification techniques, including reinforcement learning or through the use of grey-box dynamic models that can be calibrated for an individual robot.

## Force Measurements

Force characterization of the milliDelta in the vertical direction is performed using a single-axis force sensor as shown in Fig. 8. The peak forces at each height are shown in Fig. 4E, with a maximum measured force of  $13.1 \pm 0.16 \text{ mN}$  ( $n=5$ ). The vertical stiffness of the milliDelta increases with height, and is lowest near the neutral position ( $z = 0 \text{ mm}$ ), and highest near the top of its workspace ( $z = 3.5 \text{ mm}$ ). This increase in stiffness is expected as the robot approaches a kinematic singularity at the extent of its workspace. The milliDelta's force capability is sufficient for applications such as retinal microsurgery, where 75% of forces are less than 7.5 mN in magnitude (45), making it suitable for use as a tremor compensating end effector.

## Bandwidth Characterization

The frequency response of the milliDelta is experimentally measured for small displacements ( $\sim 300 \mu\text{m}$  RMS) about its neutral configuration (see Experimental Setup). A continuous linear representation (Eq. 1) of the milliDelta's dynamics near its nominal position is estimated using

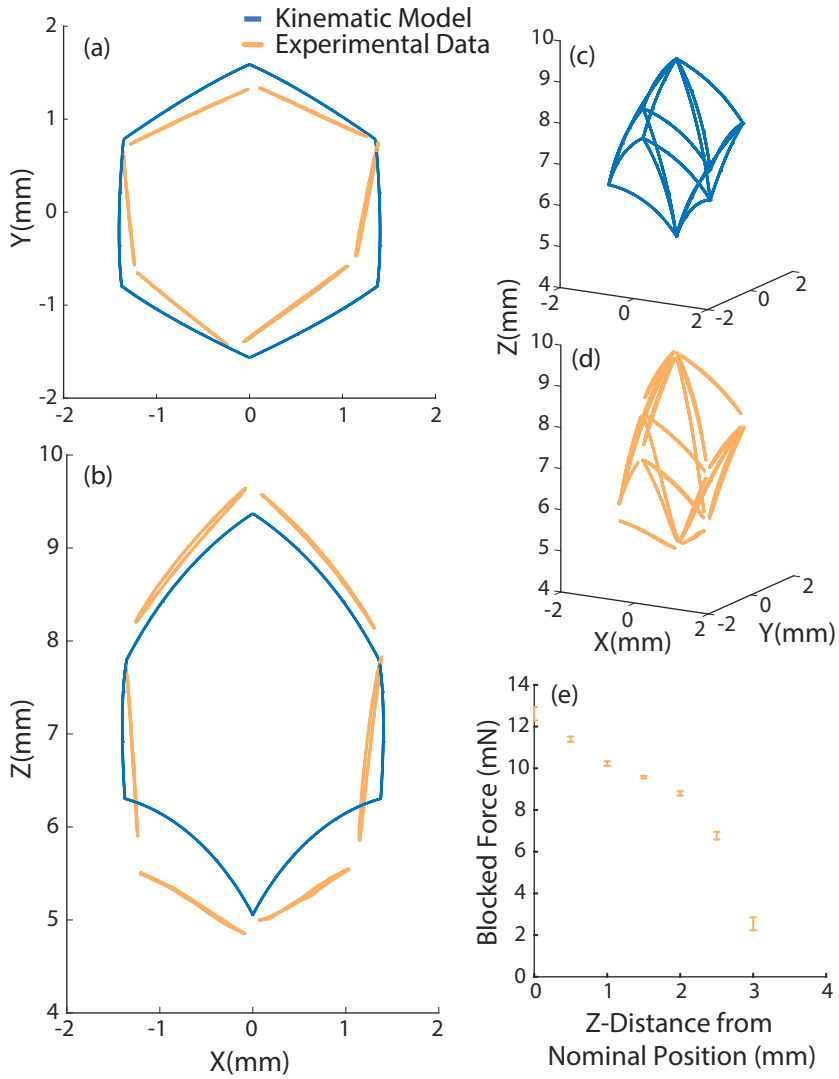


**Figure 4:** Experimental characterization of the milliDelta’s quasi-static workspace (yellow) compared with the theoretical workspace (blue) generated by the kinematic model (A-D). Outlines of the xy and xz projections of the workspaces are shown in (A) and (B). The 18 trajectories shown in (C) and (D) outline the extent of the workspace with actuator input amplitudes selected to avoid collision between linkages for all trajectories. (E) Experimental blocked force measurement in the vertical (z) direction as a function of vertical distance from the center of the workspace. The stiffness increases as the milliDelta approaches the extent of its workspace.

subspace methods (46). The state  $\vec{x}$  is prescribed to be six dimensional as the robot is a three DOF second order dynamical system. The 3D position of the output stage is used as the output vector,  $\vec{y} = (x, y, z)$ , and the three drive voltages form the input vector,  $\vec{u} = (V_1, V_2, V_3)$ . No restrictions were placed on the matrices  $A$ ,  $B$ , and  $C$ .

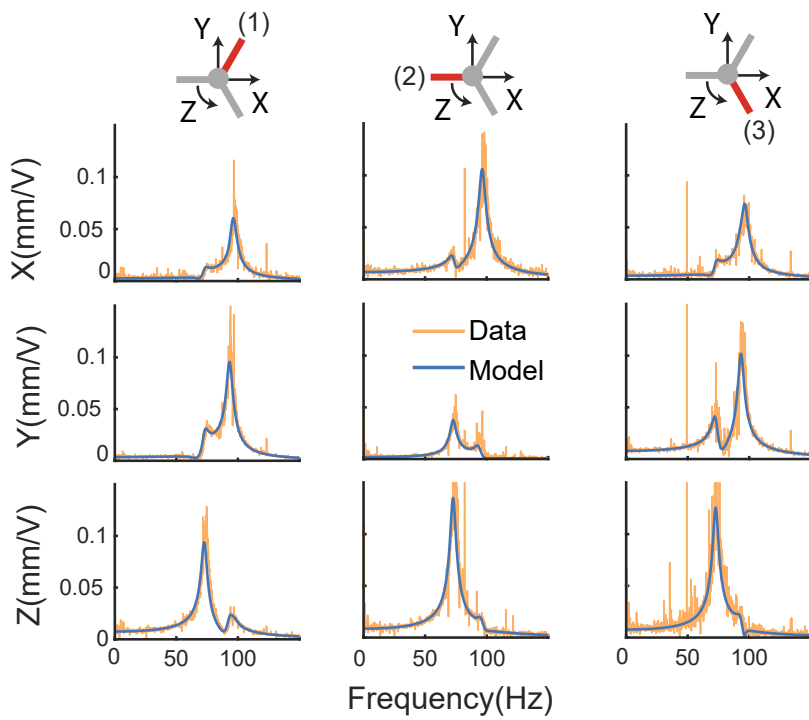
$$\begin{aligned}\frac{\partial \vec{x}}{\partial t} &= A\vec{x} + B\vec{u} \\ \vec{y} &= C\vec{x}\end{aligned}\tag{1}$$

Fig. 5 illustrates the magnitude response of the  $3 \times 3$  transfer function matrix  $H(j\omega)$  (Eq. 2) of the estimated linear system, which is compared against the experimental magnitude response of the output stage with each arm actuated individually.

$$H(j\omega) = C(j\omega I - A)^{-1}B\tag{2}$$

The linear system accurately represents the experimental magnitude response in this region, with an average position error of  $32 \pm 1 \mu m$  RMS ( $\sim 10\%$  of the region) computed for the three single arm actuations. The symmetries in the milliDelta's dynamics are easily identified in the magnitude response plots; for example, all three arms have similarly shaped magnitude responses in the z-direction. Furthermore, arms one and three are symmetric and have a similar response in all three directions. Arm two is aligned with the x-axis and displays relatively little motion in the y-direction.

The operational envelope of the milliDelta and the resonant modes are shown in a singular value plot of  $H(j\omega)$  (Fig. S3). Despite the addition of a tracking marker ( $\sim 18\%$  of the milliDelta's linkage mass), the resonant modes of this system are between 75 Hz and 95 Hz, allowing the robot to operate at frequencies up to 75 Hz without accounting for resonant behavior.



**Figure 5:** Magnitude response,  $|H(j\omega)|$ , of the milliDelta's output stage for small perturbations in the Cartesian directions (rows) for each arm (columns). The estimated linear system is shown in blue, and experimental magnitude response is shown in orange. Resonant modes, with the addition of a tracking marker, are between 75 and 95 Hz.

## Discussion

In this paper, we present the design, modeling, fabrication, and characterization of the milliDelta (430 mg mass, 15 mm×15 mm×20 mm size) driven by piezoelectric bending actuators. The milliDelta is able to achieve high precision at frequencies 10× higher than any currently available Delta robot without complex sensing and control, which is difficult to implement at the millimeter scale. More generally, the milliDelta illustrates that mechanisms found in conventional Delta robots can be realized at the millimeter scale using laminate design, PC-MEMS techniques, assembly scaffolds, and high power density actuators. These design and fabrication choices and the use of high performance composite materials result in a compact device that improves on the advantages of conventional Delta robots, including high precision, bandwidth, and payload.

To demonstrate the milliDelta’s ability to perform complex trajectories necessary for micro-manipulation and micro-scale pick-and-place, the kinematic model is used to generate input signals for planar circle, star, and H trajectories (Fig. 6, Movie S2) at 1 Hz. The robot’s motion is compared against the desired output, and the precision and accuracy across cycles ( $n=5$ ) is tabulated in Table 2. At low frequencies, the milliDelta is able to repeat trajectories with an average RMS deviation from the mean trajectory (RMS precision) down to  $1.9 \pm 0.5 \mu\text{m}$  ( $n=5$ ). Furthermore, an average RMS deviation from the desired trajectory (RMS accuracy) as low as  $24.7 \pm 0.2 \mu\text{m}$  ( $n=5$ ) is achieved. The small-deflection linear dynamic model (see Bandwidth Characterization) is inverted to allow the robot to create a star trajectory at 20 Hz with a RMS accuracy of  $68.6 \pm 0.4 \mu\text{m}$  ( $n=5$ ) and a RMS precision of  $5.2 \pm 0.9 \mu\text{m}$  ( $n=5$ ). These values demonstrates the milliDelta’s ability to perform motions necessary for pick-and-place at a frequency higher than that of any currently available Delta robot. For smooth motions, it can operate at even higher frequencies and can create a planar 1.5 mm diameter circle at its lowest

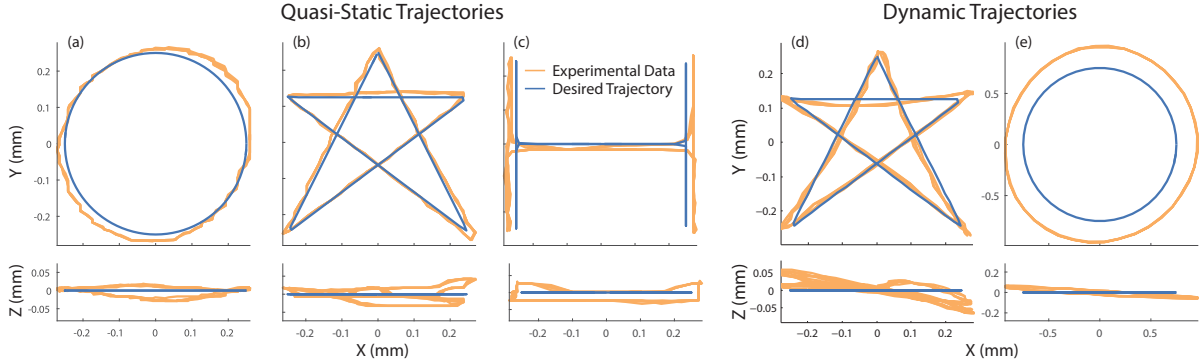


**Figure 6:** Left: quasi-static (1 Hz) experimental (orange) and desired (blue) trajectories for a 0.5 mm length planar circle (A), star (B), and H (C). Control inputs are determined using the kinematic model (see Kinematic Model). Right: high-bandwidth experimental (orange) and desired (blue) trajectories for a 0.5 mm length star executed at 20 Hz (D) and a 1.5 mm diameter circle executed at 75 Hz (E). Control inputs are determined using the estimated linear dynamic model (see Bandwidth Characterization).

**Table 2:** Trajectory Following Results. RMS precision and accuracy are calculated over five cycles of data recorded at 100 frames per cycle.

| Trajectory | Frequency (Hz) | Length ( $\mu\text{m}$ ) | RMS Precision ( $\mu\text{m}$ ) | RMS Accuracy ( $\mu\text{m}$ ) |
|------------|----------------|--------------------------|---------------------------------|--------------------------------|
| Circle     | 1              | 500                      | $2.3 \pm 1.1$                   | $34.9 \pm 0.1$                 |
| Star       | 1              | 500                      | $1.9 \pm 0.5$                   | $24.7 \pm 0.2$                 |
| H          | 1              | 500                      | $2.4 \pm 0.8$                   | $33.2 \pm 0.2$                 |
| Star       | 20             | 500                      | $5.2 \pm 0.9$                   | $68.6 \pm 0.4$                 |
| Circle     | 75             | 1500                     | $4.3 \pm 1.4$                   | $211.9 \pm 1.4$                |

resonant frequency of 75 Hz (Fig 6E, Movie S1). The output stage moves with a linear velocity of  $\sim 0.45$  m/s and experiences accelerations of  $220$  m/s $^2$  ( $\sim 22g$ ) while tracing this circle. The RMS accuracy for this high frequency trajectory decreases to  $211.9 \pm 1.4$   $\mu\text{m}$  ( $n=5$ ), but a RMS precision of  $4.3 \pm 1.4$   $\mu\text{m}$  ( $n=5$ ) is maintained. This degradation in accuracy is due to the failure of the linear model to capture the non-linear dynamics that manifest themselves as the output stage moves away from its neutral position. Overall, the milliDelta's ability to perform given trajectories at increasing frequencies with high RMS precision and accuracy establishes its utility for micromanipulation tasks.

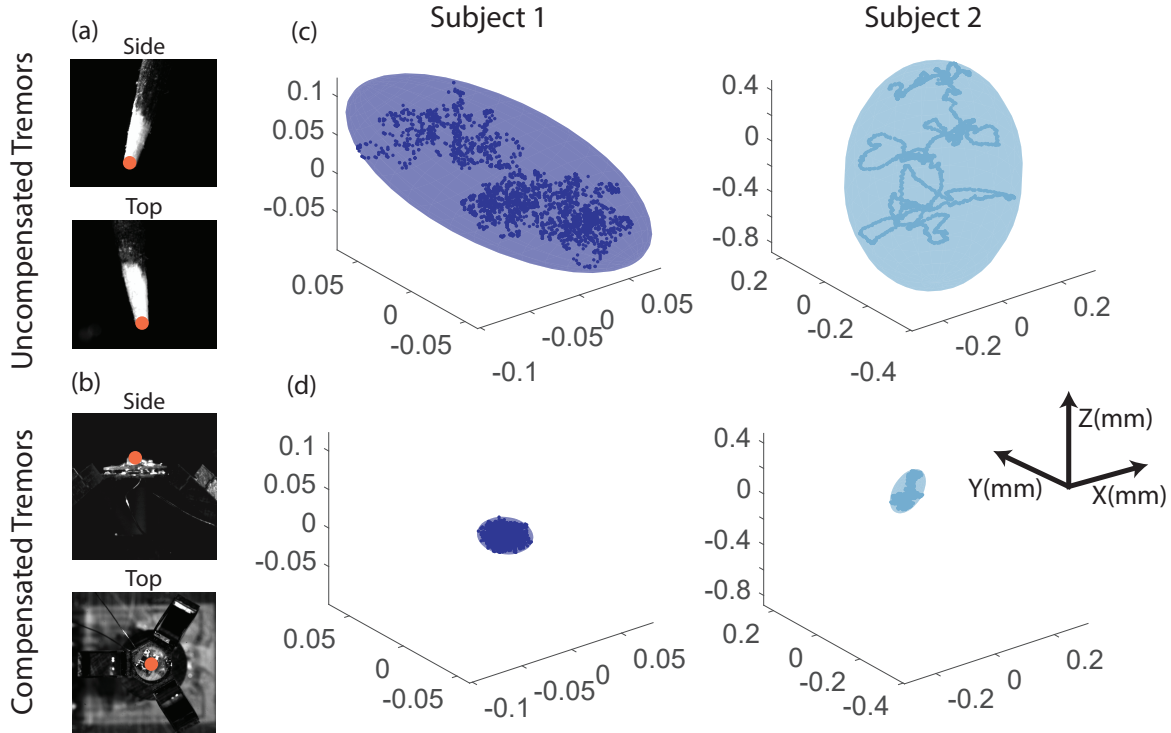


**Figure 7:** Experimental results for tremor reduction. Orthogonal camera views used to record hand tremors (A) and milliDelta motion (B) are shown with a red circle denoting the tracked point. (C) Tremor data for two subjects is shown with bounding ellipsoids. The linear model is inverted to allow the milliDelta to track the measured tremors, and the tracking error is shown with bounding ellipsoids (D). The milliDelta is able to reduce hand tremor magnitudes by 81% RMS.

Leveraging the milliDelta’s high precision and bandwidth, we also demonstrate its potential for tremor compensation in surgical or assembly operations (see Movie S3). Typical hand tremors range from  $\sim$ 8–12 Hz and are  $50\text{ }\mu\text{m}$  peak-to-peak in each of the principal axes (47–50), which falls well within the milliDelta’s operational envelope. Hand tremors are measured for three subjects (two shown in Fig. 7 and Movie S3 for clarity) attempting to hold a visual marker in place. The estimated linear model is inverted offline to determine the input trajectory that allows the robot to track the hand tremors. The resulting motion of the milliDelta is recorded and the tracking error is computed. The RMS tracking error averaged over all three subjects is  $81 \pm 4$  percent smaller than the RMS tremor amplitude, which demonstrates the milliDelta’s ability to successfully mitigate hand tremors. Additionally, the robot’s small form-factor and low mass make it a suitable end effector for existing devices.

The design of the milliDelta can also be further optimized for tremor mitigation or micro-manipulation. For example, the smaller workspace required for tremor mitigation would allow for a significantly lower transmission ratio, improving payload capacity and reducing the robot’s size and mass. The current mounting system can also be easily modified for incorporation with existing devices as an end effector. Alternatively, the linkages and actuators can be redesigned to increase the workspace for micro-manipulation tasks. Utilizing the design and fabrication methodology described here, the milliDelta can be reconfigured for an application with specific design requirements (i.e., workspace, precision, bandwidth, payload). Overall, the milliDelta exemplifies the advantages of scaling down parallel mechanisms, and the PC-MEMS process combined with the use of high power density actuators can be applied to other widely used parallel manipulators for high performance at small scales.

# Materials and Methods

## Kinematic Model

The milliDelta's kinematics deviate slightly from that of a conventional Delta robot due to design modifications (see Design) that enable fabrication at the millimeter scale. Consequently, the forward and inverse kinematics are computed using MATLAB's multibody simulation environment (Simscape Multibody). Each link is modeled as shown in Fig. S1 with geometric parameters (Table S1) taken from the 3D CAD model. Kinematic transformations between links are defined using a zero DOF weld joint to represent rigid connections between links, and a one DOF revolute joint for flexures. One DOF prismatic joints between each transmission linkage and the world frame represent the linearized deflections of the three actuators. Loop constraints are enforced at the output stage. Inputs for forward kinematics are the actuator deflections, and the outputs are the Cartesian position of the center of the output stage. For the inverse kinematics, a three DOF Cartesian joint between the center of the output stage and world frame is used to input different trajectories, and the linearized actuator deflections are recorded as outputs.

## Manufacturing the milliDelta

The rigid layers of the milliDelta are formed by curing three sheets of single layer carbon fiber (Q1-112, Tohotenax) together at orthogonal angles, yielding a final composite with a thickness of  $\sim 100 \mu\text{m}$ . A  $12.5 \mu\text{m}$  polyimide film (Kapton, DuPont) is used for the flexible layers to generate the flexures, and heat and pressure activated sheet adhesive (Pyralux FR1500, DuPont) bonds each layer of the laminate. Each layer is individually cut using a laser micromachining system (Oxford Lasers) as shown in Fig. S2A. After each layer is cut, the carbon fiber and polyimide are ultrasonically cleaned with isopropyl alcohol, plasma etched (Diener) for enhanced bonding, aligned laterally for lamination using precision dowel pins, and then cured together using heat and pressure (Fig. S2B). The resulting laminate is laser micromachined to release the

structure from the surrounding bulk material (Fig. S2B). In order to improve assembly, the milliDelta is placed in a custom jig that fixes the linkages in the desired neutral state and constrains the moving flexures. Once in this configuration, the fixed flexures are glued to ensure that the robot is properly aligned and that the moving flexures remain unloaded in the neutral configuration (Fig. S2C). This assembly fixture enables rapid design iterations, but some assembly errors still occur. Once a mature design is reached, a pop-up approach to fabrication (44) can be used to further automate folding, improve linkage alignment, and eliminate manual assembly.

Once released from the assembly scaffold, the milliDelta is attached to three piezoelectric bending actuators, which are aligned using a custom 3D printed base (Stratsys). The piezoelectric bending actuators are fabricated using the materials and techniques described in (29), but with the substitution of 25  $\mu\text{m}$  copper-clad polyimide film (Dupont) for the bridges. The 3D printed base serves as mechanical ground for the actuators and the milliDelta's base stage, and houses the routing circuitry. Power and control signals are generated off-board and are delivered via a five-wire tether.

## Experimental Setup and Procedure

The experimental setup in Fig. 8 is used to determine the workspace and frequency response, as well as perform tremor compensation and path following. The milliDelta is fixed to a micropositioning stage (Thorlabs) and centered in the fields of view of two orthogonally positioned high speed cameras (Phantom v7.3) with a spatial resolution of  $\sim 30 \mu\text{m}$  per pixel. The motion of the milliDelta is tracked using vision-based tracking (Xcitex-ProAnalyst) with sub-pixel accuracy. The cameras are time synced through an xPC target system (Mathworks), and calibrated using the Camera Calibration Toolbox for MATLAB to provide the 3D position of the milliDelta.

The experimental setup (Fig. 8) is modified for the blocked force measurements as follows: a single axis force sensor (Futek LSB200) is positioned above the milliDelta on a microposi-

tioning stage (Thorlabs), and the high speed cameras are not used.

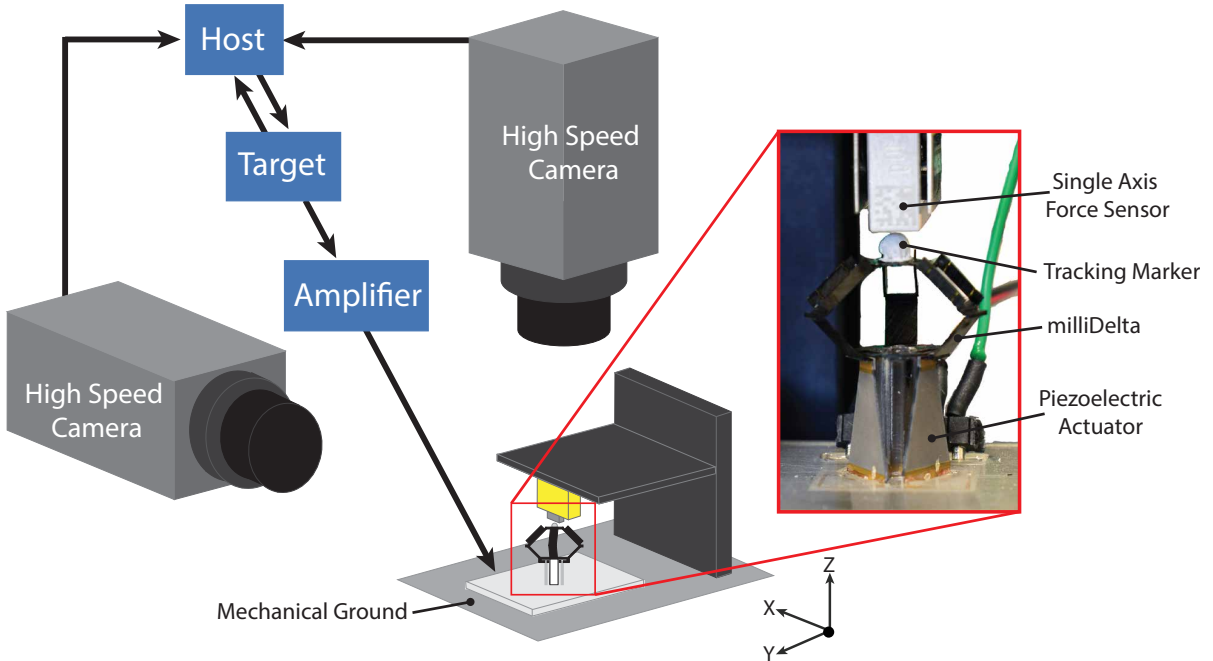


**Figure 8:** Experimental setup for workspace, bandwidth, and force characterization of the milliDelta. Two orthogonal, synced, high-speed cameras are centered on the milliDelta. A reflective marker is placed on the output stage and its position is tracked using vision-based techniques. For force testing, a single-axis force sensor that obscures the top camera is positioned above the milliDelta. The cameras, force sensor, and milliDelta are controlled in real time using MATLAB's xPC target system.

## Workspace

To determine the volume of the milliDelta's workspace, each arm is actuated individually with the other two arms fixed at their extreme positions (12 trials). Additionally, pairs of arms are actuated together with the inactive arm fixed at its extreme positions (six trials). For each of the eighteen actuation schemes tested, the actuators are driven by 100 V peak-to-peak, 2 Hz sinusoidal signals. Higher input voltages would have resulted in linkage collisions for certain actuation schemes. Eight cycles of data is recorded for each scheme at 50 frames per cycle

(fpc), corresponding to 100 frames per second (fps).

### **Blocked Force Measurements**

Blocked force is measured in the vertical direction by driving all three actuators with a 200 V peak-to-peak, 1Hz sinusoidal signal. The force sensor is positioned directly above the milliDelta, and is moved upwards at increments of  $500 \mu\text{m}$  until the output stage no longer contacts the sensor. Five cycles of force data are recorded at each height.

### **Frequency Response**

The frequency response is measured by exciting each arm with independently generated band-limited (200 Hz) white noise voltages with RMS amplitudes of  $\sim 5.5$  V. The motion of the milliDelta is recorded at 4000 fps for 10 seconds.

### **Trajectory Following**

Desired actuator input deflections are generated using the kinematic model for the three quasi-static (1 Hz) trajectories, and signal amplitudes are selected to match these deflections. Data is recorded at 100 fps for five cycles. The estimated dynamic model is inverted to generate inputs for the 20 Hz star and 75 Hz circle. The motion of the milliDelta is recorded at 100 fpc (2000 fps) and 40 fpc (3000 fps), respectively, for five cycles.

### **Tremor Compensation**

The estimated dynamic model is inverted in a post-processing step to allow the milliDelta to track the recorded hand tremors. The hand tremors and milliDelta motions are recorded at 400 Hz for eight seconds. Hand tremors are measured for three subjects holding a visual marker (toothpick), approximating the frequency and magnitude of tremors measured during micro-surgery (47–50). The raw hand tremor position data is filtered using an acausal second-order

low-pass Butterworth filter with a cutoff frequency of 50 Hz before the inverse dynamics are calculated.

## Acknowledgments

Thank you to Dr. Merve Acer, Dr. Benjamin Goldberg, Elizabeth Helbling, Dr. Kaushik Jayaram, and all members of the Harvard Microrobotics Laboratory for their advice and assistance.

**Funding:** This work is partially funded by the Wyss Institute for Biologically Inspired Engineering and the National Defense Science and Engineering Graduate Fellowship. In addition, the prototypes were enabled by equipment supported by the ARO DURIP program (award #W911NF-13-1-0311). Any opinions, findings, and conclusions or recommendations expressed in this material are those of the authors and do not necessarily reflect the views of the National Science Foundation.

**Author Contributions:** FZT, JK, and RJW initiated the project. HM, FZT, ND designed and conducted the research, and all authors contributed to the development of the project and preparation of the manuscript.

## References

1. M. Stock, K. Miller, *Transactions-American Society of Mechanical Engineers Journal of Mechanical Design* **125**, 292 (2003).
2. M. López, E. Castillo, G. García, A. Bashir, *Proceedings of the Institution of Mechanical Engineers, Part C: Journal of Mechanical Engineering Science* **220**, 103 (2006).
3. J.-P. Merlet, *Parallel Robots*, vol. 128 (Springer Science & Business Media, 2006).

4. R. Clavel, Device for the movement and positioning of an element in space (1990). US Patent 4,976,582.
5. R. Clavel (1991).
6. L.-W. Tsai, *Robot analysis: the mechanics of serial and parallel manipulators* (John Wiley & Sons, 1999).
7. L. Rey, R. Clavel, *Parallel Kinematic Machines* (Springer, 1999), pp. 401–417.
8. F. Pierrot, C. Reynaud, A. Fournier, *Robotica* **8**, 105 (1990).
9. P. Vischer, R. Clavel, *Robotica* **16**, 207 (1998).
10. P. Vischer, R. Clavel, *The International Journal of Robotics Research* **19**, 5 (2000).
11. J.-P. Merlet, *IEEE Transactions on Robotics and Automation* **9**, 842 (1993).
12. T. Brogårdh, *Annual Reviews in Control* **31**, 69 (2007).
13. E. Pernette, S. Henein, I. Magnani, R. Clavel, *Robotica* **15**, 417 (1997).
14. A. Codourey, S. Perroud, Y. Mussard, *Precision Assembly Technologies for Mini and Micro Products* pp. 193–200 (2006).
15. T. Tanikawa, et al., *Intelligent Robots and Systems, 2002. IEEE/RSJ International Conference on* (IEEE, 2002), vol. 2, pp. 1778–1783.
16. T. Tanikawa, T. Arai, *IEEE Transactions on Robotics and Automation* **15**, 152 (1999).
17. M. Salerno, A. Firouzeh, J. Paik, *Journal of Mechanisms and Robotics* **9**, 041005 (2017).
18. J. E. Correa, J. Toombs, N. Toombs, P. M. Ferreira, *Journal of Manufacturing Processes* **24**, 370 (2016).

19. S. Perroud, A. Codourey, Y. Mussard, *Proc. 5th International Workshop on Microfactories, Besancon, S2-2, P3-5* (2006).
20. Omron Adept Technologies, Inc., Kawasaki Heavy Industries, Ltd., Asyri SA, Festo, ABB.
21. A. M. Hoover, R. S. Fearing, *Robotics and Automation, 2008. ICRA 2008. IEEE International Conference on* (IEEE, 2008), pp. 886–892.
22. C. D. Onal, R. J. Wood, D. Rus, *Robotics and Automation (ICRA), 2011 IEEE International Conference on* (IEEE, 2011), pp. 4608–4613.
23. J. P. Whitney, P. S. Sreetharan, K. Y. Ma, R. J. Wood, *Journal of Micromechanics and Microengineering* **21**, 115021 (2011).
24. R. Wood, S. Avadhanula, R. Sahai, E. Steltz, R. Fearing, *Journal of Mechanical Design* **130**, 052304 (2008).
25. L. L. Howell, *Compliant Mechanisms* (John Wiley & Sons, 2001).
26. R. S. Fearing, *Tutorial on Micro Mechatronics and Micro Robotics, ICRA* **98** (1998).
27. S. Russo, T. Ranzani, C. J. Walsh, R. J. Wood, *Advanced Materials Technologies* (2017).
28. J. Kim, *Microscale Soft Robotics: Motivations, Progress, and Outlook* (Springer).
29. N. T. Jafferis, M. J. Smith, R. J. Wood, *Smart Materials and Structures* **24**, 065023 (2015).
30. K. R. Oldham, J. S. Pulskamp, R. G. Polcawich, M. Dubey, *Journal of Microelectromechanical Systems* **17**, 890 (2008).
31. D. J. Cappelleri, M. I. Frecker, T. W. Simpson, A. Snyder, *Int. J. Mach. Tools Manuf* **33**, 193 (2002).

32. W. S. Trimmer, *Sensors and actuators* **19**, 267 (1989).
33. R. J. Wood, *Intelligent Robots and Systems (IROS), 2007 IEEE/RSJ International Conference on* (IEEE, 2007), pp. 1889–1894.
34. K. L. Hoffman, R. J. Wood, *Robotics and Automation (ICRA), 2010 IEEE International Conference on* (IEEE, 2010), pp. 1196–1202.
35. A. T. Baisch, O. Ozcan, B. Goldberg, D. Ithier, R. J. Wood, *The International Journal of Robotics Research* **33**, 1063 (2014).
36. Y. Li, Q. Xu, *IEEE Transactions on Robotics* **25**, 645 (2009).
37. S. Yang, R. A. MacLachlan, C. N. Riviere, *IEEE/ASME Transactions on Mechatronics* **20**, 761 (2015).
38. A. Üneri, *et al.*, *Biomedical Robotics and Biomechatronics (BioRob), 2010 3rd IEEE RAS and EMBS International Conference on* (IEEE, 2010), pp. 814–819.
39. Y. Noda, *et al.*, *PloS one* **8**, e54116 (2013).
40. M.-O. Demaurex, *Parallel Kinematic Machines* (Springer, 1999), pp. 395–399.
41. K. Y. Ma, P. Chirarattananon, R. J. Wood, *Intelligent Robots and Systems (IROS), 2015 IEEE/RSJ International Conference on* (IEEE, 2015), pp. 1558–1564.
42. D. M. Aukes, R. J. Wood, *ASME Conference on Smart Materials, Adaptive Structures and Intelligent Systems* (2014).
43. N. Doshi, *et al.*, *Intelligent Robots and Systems (IROS), 2015 IEEE/RSJ International Conference on* (IEEE, 2015), pp. 4119–4126.

44. P. S. Sreetharan, J. P. Whitney, M. D. Strauss, R. J. Wood, *Journal of Micromechanics and Microengineering* **22**, 055027 (2012).
45. P. K. Gupta, P. S. Jensen, E. de Juan, *International Conference on Medical Image Computing and Computer-Assisted Intervention* (Springer, 1999), pp. 1218–1225.
46. P. Van Overschee, B. De Moor, *Subspace identification for linear systems: Theory - Implementation - Applications* (Springer Science & Business Media, 2012).
47. C. N. Riviere, R. S. Rader, N. V. Thakor, *IEEE Transactions on Biomedical Engineering* **45**, 839 (1998).
48. S. Singhy, C. Riviere, *Bioengineering Conference, 2002. Proceedings of the IEEE 28th Annual Northeast* (IEEE, 2002), pp. 171–172.
49. W. T. Ang, P. Pradeep, C. Riviere, *Engineering in Medicine and Biology Society, 2004. IEMBS'04. 26th Annual International Conference of the IEEE* (IEEE, 2004), vol. 1, pp. 2738–2741.
50. R. Elble, W. Koller, *Tremor, Johns Hopkins Series in Contemporary Medicine and Public Health* (Johns Hopkins University Press, Baltimore, MD, 1990).
51. D. E. Kirk, *Optimal control theory: an introduction* (Courier Corporation, 2012).

**Table 3:** Link length parameters of the milliDelta, piezoelectric bending actuator dimensions, and flexure stiffnesses (all flexures have the same dimensions). Length  $L_3$  determines the transmission ratio of the milliDelta.

| Parameter   | Value |
|---|-------|
| $L_1$ (mm)  | 0.65  |
| $L_2$ (mm)  | 0.65  |
| $L_3$ (mm)  | 0.45  |
| $L_4$ (mm)  | 5.66  |
| $L_5$ (mm)  | 3.90  |
| $D_{ra}$ (mm)   | 0.80  |
| PZT Thickness ( $\mu\text{m}$ )                             | 135   |
| CF Thickness ( $\mu\text{m}$ )                              | 50    |
| PZT Length (mm)   | 9.69  |
| Nominal Width (mm)  | 5.26  |
| Extension Length (mm)                                       | .92   |
| Width Ratio   | 1.5   |
| Flexure Stiffness ( $\mu\text{N}\cdot\text{m}/\text{rad}$ ) | 11.6  |

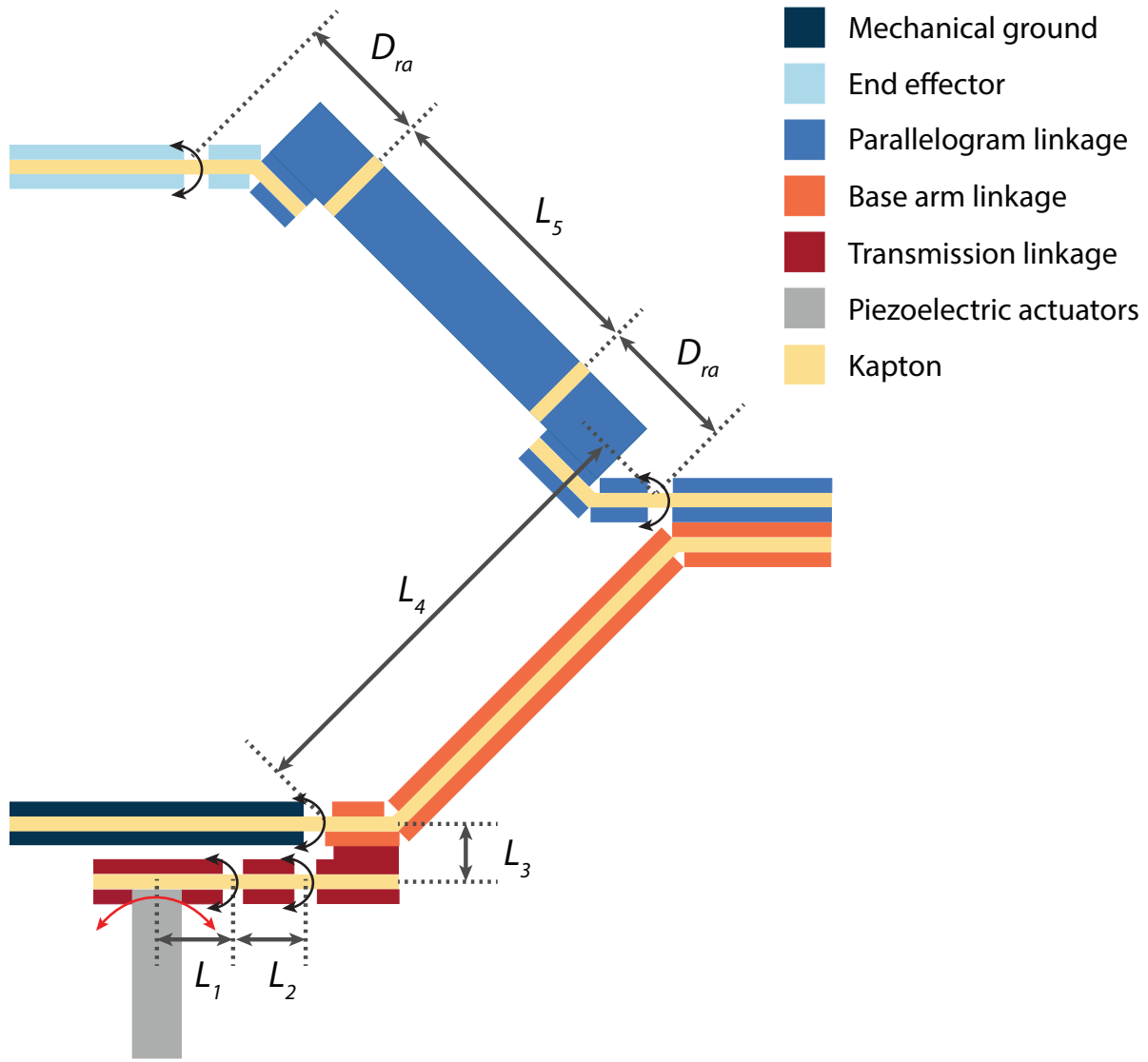


**Figure 9:** Relevant linkage parameters (with corresponding values in Table S1) for one arm of the milliDelta. The input motion of the piezoelectric bending actuator is represented with a curved red arrow and the resulting flexure motions are represented with curved black arrows. The composite laminate structure is shown with the flexible polyimide and rigid layers as described in the legend. The parameter  $D_{ra}$  represents the axis bias between the two perpendicular revolute joints used to approximate a universal joint. Linkage length  $L_3$  determines the transmission ratio of the milliDelta.

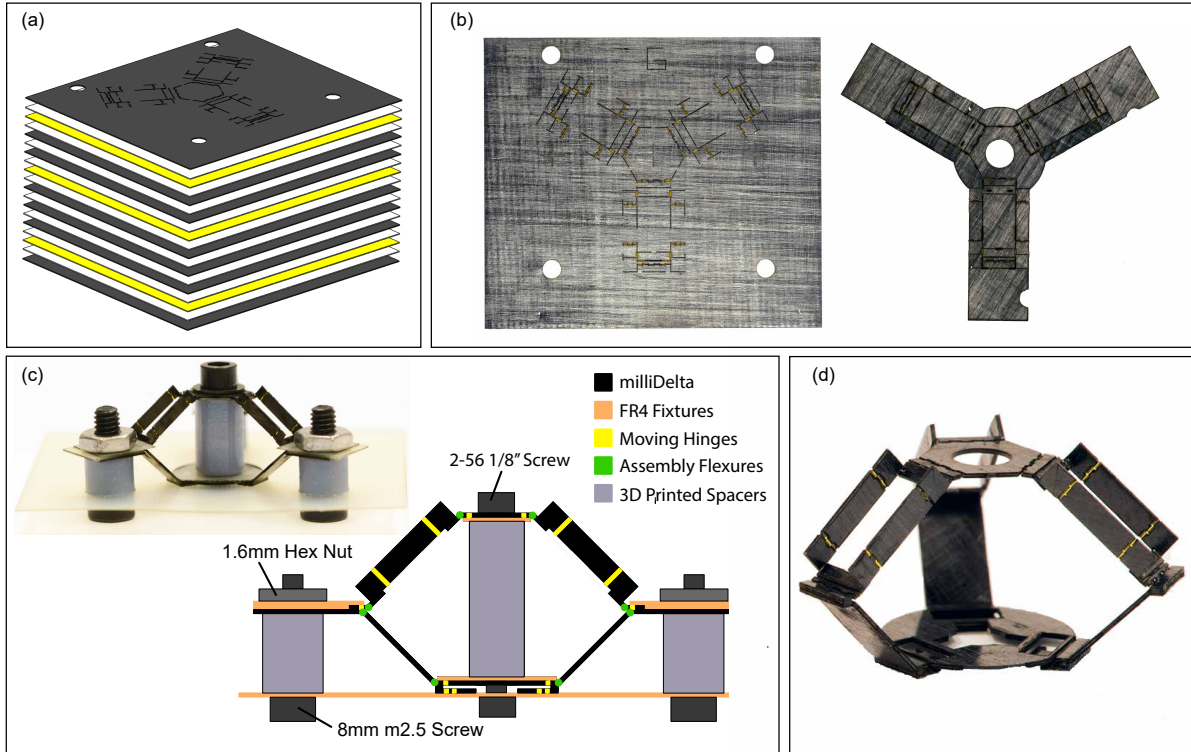


**Figure 10:** Manufacturing process for the milliDelta. (A) Cut files for the 19 constituent layers designed in *popupCAD*. Each layer is laser machined, and the layers are aligned using dowel pins and laminated using a heat and pressure (B, left). The laminated structure is laser machined to release the mechanism from the surrounding bulk material (B, right). A schematic and image of the jig used to fixture the milliDelta during manufacturing for improved alignment is shown in (C). Fiberglass sheets are used to clamp moving flexures in a neutral state and align linkages, and the assembly flexures are glued in place. The finished device in its neutral position before attaching to piezoelectric bending actuators is shown in (D).

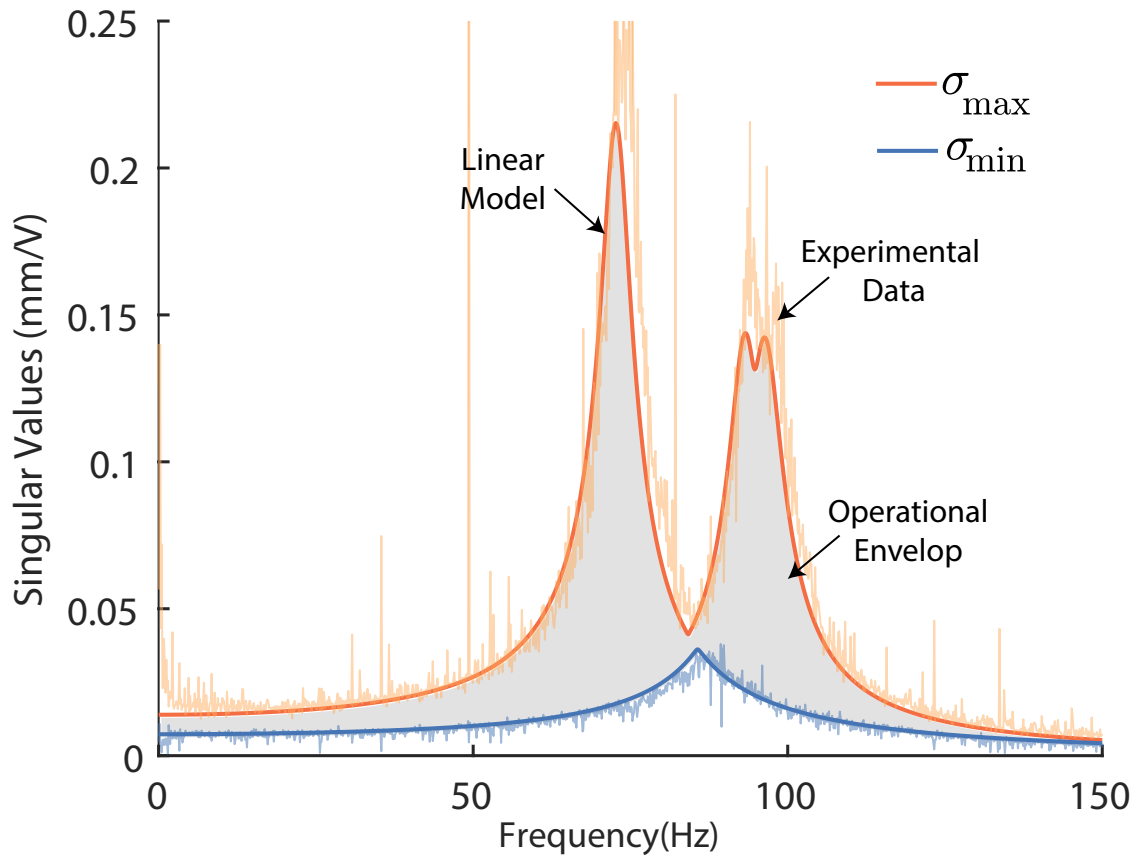


**Figure 11:** Plots of the maximum (orange) and minimum (blue) singular values of the transfer function matrix,  $H(j\omega)$ , as a function of frequency. The linear model and experimental data are labeled. The region between the singular values (shaded in gray) is the operational envelope of the milliDelta, and can be considered as the bounding region for the nine magnitude responses plotted in Fig. 5 (5I)